Nanoscale Advances

ROYAL SOCIETY OF CHEMISTRY | Celebrating IYPT 2019

PAPER
Li Chen, Zheng Guo *et al.*
Enhanced chemiresistive sensing performance
of well-defined porous CuO-doped ZnO nanobelts
toward VOCs

NCNST

PAPER

Check for updates

Enhanced chemiresistive sensing performance of well-defined porous CuO-doped ZnO nanobelts toward VOCs†

Gang Li,‡[ab] Yao Su,‡[b] Xu-Xiu Chen,[a] Li Chen,*[a] Yong-Yu Li[ab] and Zheng Guo (ID) *[ab]

Although the post-doping approach as a typical and effective method has been widely employed to improve the gas sensing performance of nanostructured metal oxides, it easily breaks their porous nanostructures. Herein a facile partial cation-exchange strategy combined with thermal oxidation has been developed to prepare porous CuO-doped ZnO nanobelts. Using $ZnSe \cdot 0.5N_2H_4$ nanobelts as the precursor template, Cu_2Se-doped precursor nanobelts were obtained with Zn^{2+} cations partially exchanged by Cu^{2+} cations. After annealing in air, they are further oxidized into well-defined porous CuO-doped ZnO nanobelts. Through manipulating the amount of exchanged Cu^{2+} cations, the CuO-doping concentration can be precisely tuned. Based on the assembly approach and *in situ* thermal oxidation, a uniform and stable sensing film consisting of porous CuO-doped nanobelts was fabricated. Compared with pristine porous ZnO nanobelts, the as-prepared porous CuO-doped nanobelts with p-type CuO|n-type ZnO heterojunctions exhibited better sensing performance toward volatile organic compounds (VOCs). Especially for 3 at% CuO-doped porous ZnO nanobelts, the relative responses toward 100 ppm of ethanol, acetone and formaldehyde were greatly enhanced more than two, four and ten times, respectively. Due to the porous structure, they also displayed a fast response/recovery time. Finally, this enhanced sensing mechanism was discussed for porous CuO-doped ZnO nanobelts.

Introduction

Attributed to the large active surface-to-volume ratios and more channels favoring the diffusion of gas/solution, porous nanostructures are of considerable interest and exhibit extensive applications, especially in the field of gas sensors.[1] Compared with those of the solid nanostructures of metal oxides, the sensing performances of their porous nanostructures, such as sensitivity, response/recovery time, *etc.*, are greatly enhanced. Among the previously reported porous nanostructures, ZnO as a typical gas sensing material has received great attention.[2] To date, various porous ZnO nanostructures (nanospheres, nanowires, nanotubes, nanosheets, nanobelts, *etc.*) have been prepared and demonstrated to exhibit excellent sensing performances.[3] As is well-known, modification and post-doping methods are generally regarded as two typical approaches to further improve the sensitivity and selectivity of metal oxides. In this view, many porous ZnO nanostructures have been commonly modified with noble metal nanoparticles such as Au, Ag, Pt, Pd, *etc.*[4] Indeed, their sensitivity and selectivity toward some VOCs has been improved. However, few reports involve preparing metal oxide-doped porous ZnO nanostructures *via* the post-doping approach.[5] The main reason is that their porous nanostructures can easily be broken. Therefore, it is still necessary to develop a new approach to overcome this disadvantage.

Belt-like nanostructures as a promising building-block are of great benefit to nanoelectronics and nanosensors.[6] Endowed with a porous structure, their intrinsic characteristics can be promisingly enhanced, especially for gas-sensing performances.[6c] Recently, ZnO nanobelts with a porous structure have also entered into the scope of scientific research.[7] By our group, porous ZnO nanobelts have been successfully derived from $ZnSe \cdot 0.5N_2H_4$ nanobelts *via* a thermal oxidation method.[3d] Moreover, they present high sensitivity with a fast response/recovery time toward VOCs. In addition, $ZnSe \cdot 0.5N_2H_4$ nanobelts as the precursor template can be further transformed into other selenide nanobelts *via* a complete cation-exchange reaction. After complete exchange with Ag^+ and Cd^{2+} cations, they can be converted into Ag_2Se and CdSe nanobelts, respectively.[8] Similarly, Cu_2Se nanobelts have also been prepared through complete exchange with Cu^{2+} cations. Notably, the as-prepared Cu_2Se nanobelts can be further transformed into porous CuO nanobelts after calcination in air.[9] In fact, the partial cation-

[a] *Institutes of Physical Science and Information Technology, Anhui University, Hefei 230601, People's Republic of China. E-mail: lichen@ahu.edu.cn; zhguo@ahu.edu.cn*

[b] *Key Laboratory of Environmental Optics and Technology, Institute of Intelligent Machines, Chinese Academy of Sciences, Hefei 230031, People's Republic of China*

† Electronic supplementary information (ESI) available. See DOI: 10.1039/c9na00163h

‡ G. Li and Y. Su contributed equally to this work.

exchange approach has been demonstrated to be a facile and effective route to doped nanomaterials, especially for nanostructured chalcogenides. Through employing ZnX nanostructures (X = S, Se, Te) as precursor template, doped nanostructures have been widely obtained after partial exchange with other metal cations.[10] Due to the fact that chalcogenides can easily be oxidized in air under thermal treatment, the partial cation-exchange approach along with thermal oxidation can offer a new route to prepare metal oxide-doped porous ZnO nanobelts.

To demonstrate the above idea, herein a partial cation-exchange reaction between $ZnSe \cdot 0.5N_2H_4$ nanobelts and Cu^{2+} cations has been employed in combination with thermal oxidation as an example to prepare well-defined porous CuO-doped ZnO nanobelts. The whole synthetic process is shown in Scheme 1. After partial exchange with Cu^{2+} cations, first Cu_2Se-doped precursor nanobelts are obtained. After annealing in air, they are further oxidized into porous CuO-doped ZnO nanobelts. Compared with those of pristine porous ZnO nanobelts, their sensing performances toward typical VOCs have been greatly enhanced, especially toward ethanol, acetone and formaldehyde. Promisingly, this work can be extended to prepare other metal oxide-doped porous ZnO nanostructures with enhanced gas-sensing performance.

Experimental section

Chemical reagents

All chemical reagents used were analytical grade and purchased from Shanghai Chemical Reagent Co., Ltd. (China). And they were used as received without further purification. Milli-Q water with a resistivity greater than 18.0 MΩ cm was used in the preparation of aqueous solutions.
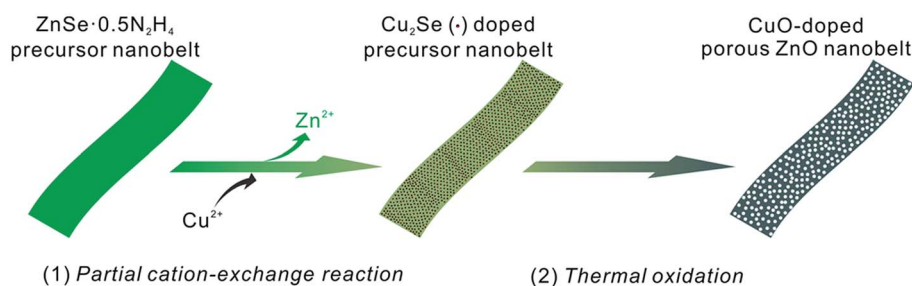
Synthesis of porous CuO-doped ZnO nanobelts

According to our previous report, $ZnSe \cdot 0.5N_2H_4$ nanobelts as a precursor template were first synthesized through a facile hydrothermal approach.[3d] Afterwards the obtained precursor nanobelts (0.2 mmol) were dispersed into 20 mL aqueous solution containing 0.4 g poly(vinylpyrrolidone) (PVP, K30) surfactant. Under magnetic stirring for 10 minutes, a homogeneous solution was formed. Subsequently, a solution (10 mL)

containing a certain amount of $Cu(NO_3)_2$ was added dropwise into the above homogeneous solution. To facilitate the partial exchange of added Cu^{2+} cations, it was continuously stirred for 5 h at room temperature. Then Cu_2Se-doped precursor nanobelts were obtained after centrifugation and washed with DI water several times. Finally the as-prepared Cu_2Se-doped precursor nanobelts were calcined in air at 500 °C (with a low heating rate of 2 °C min^{-1} from room temperature) for 2 h. After cooling down to room temperature, porous CuO-doped ZnO nanobelts were achieved. Through manipulating the exchanged amount of Cu^{2+} cations, porous ZnO nanobelts with a series of corresponding CuO-doping amounts were obtained. The ZnO nanobelts with 1, 2, 3, 4, and 5 at% CuO-doping amounts were denoted as CZ-1, CZ-2, CZ-3, CZ-4 and CZ-5, respectively.

Fabrication and measurements of gas-sensing devices

To fabricate the gas sensing devices from porous CuO-doped ZnO nanobelts, an assembly technique combined with *in situ* calcination was performed to prepare a uniform and stable sensing film. First, the as-prepared Cu_2Se-doped precursor nanobelts were assembled to form a uniform and dense film according to our previously reported approach.[8a] Then alumina ceramic tubes (4 mm × 1 mm, length × diameter) with two Au electrodes on their outer surface were employed as substrates. After being dipped and pulled into the above assembled film several times, the alumina ceramic tubes were covered with a uniform and dense film consisting of Cu_2Se-doped precursor nanobelts. Following the above-mentioned thermal conversion approach, they were *in situ* transformed into a uniform and porous CuO-doped ZnO nanobelt sensing film on the surface of alumina ceramic tubes. The gas-sensing performance of the porous CuO-doped ZnO nanobelts was measured on a Keithley 6487 picoammeter/voltage sourcemeter acting as both the voltage source and current reader, which was connected with the two Au electrodes. A Ni–Cr resistor (30 Ω) as a heater was employed to provide the working temperature inside the alumina ceramic tubes. All gas-sensing measurements were performed with our previously reported setup and program in dry air.[1c] The relative response is defined as $S = R_g/R_a$, where R_a is the resistance of the sensing film in dry air and R_g is that in dry air mixed with the detected gases. In addition, the response time (τ_{res}) and recovery time (τ_{rec}) are defined as the time taken

Scheme 1 The process of preparation of porous CuO-doped ZnO nanobelts: (1) Zn^{2+} cations of $ZnSe \cdot 0.5N_2H_4$ nanobelts as a precursor template partially exchanged by Cu^{2+}, (2) the transformation from Cu_2Se doped precursor nanobelts to porous CuO-doped ZnO nanobelts *via* thermal oxidation.

for the gas sensor to achieve 90% of the total response change with the exposure and evacuation of the detected gases, respectively.

Characterization

Scanning electron microscopy (SEM, ZEISS AURIGA) and transmission electron microscopy (TEM) (JEOL-2010 transmission electron microscope) coupled with energy-dispersive X-ray spectroscopy (EDX) and selected area electron diffraction (SAED) were employed to characterize the morphologies and microstructures of the as-prepared samples. Their X-ray diffraction (XRD) patterns were obtained on a Philips X'pert diffractometer (X'Pert Pro MPD) with Cu Kα radiation (1.5418 Å). X-ray photoelectron spectroscopy (XPS) measurements were performed with a VG ESCALAB MKII spectrometer using an Mg Kα X-ray source (1253.6 eV, 120 W). Additionally, the doping amount of the Cu element was measured by using inductively coupled plasma mass spectrometry (ICP-MS, PlasmaQuad 3, USA).

Results and discussion

Consistent with the previous report, the as-prepared $ZnSe \cdot 0.5N_2H_4$ nanobelts are relatively uniform.[3d] As shown in Fig. 1a, their length is up to several tens of micrometers, and their width mainly ranges from 100 to 200 nm. After partial exchange with Cu^{2+} cations (5 at%), their initial belt-like morphologies are well preserved, which can be seen in Fig. 1b. Similar to the cation-exchange synthesis of Cu_2Se, the morphological preservation is ascribed to the confining effect of the PVP surfactant coating layer.[9] With the complete doping of the added Cu^{2+} cations, they then form Cu_2Se-doped precursor nanobelts. Inspired by the thermal transformation from precursor nanobelts to porous ZnO nanobelts and Cu_2Se nanobelts to porous CuO nanobelts, a similar approach is further performed to convert Cu_2Se-doped precursor nanobelts into well-defined porous CuO-doped ZnO nanobelts.[3d,9] As presented in Fig. 1c, the belt-like morphology is still maintained after calcination at 500 °C in air. In the magnified SEM image shown in Fig. 1d, it can clearly be seen that a porous structure emerges. This result can be further confirmed from the TEM image displayed in Fig. 1e. Fig. 1f shows XRD patterns of the as-prepared porous nanobelts. Besides the diffraction peaks of ZnO, two other weak peaks emerge, which can be indexed to CuO. This result is different from our previous report that Ag_2Se-doped precursor nanobelts are converted to Ag nanoparticle decorated porous ZnO nanobelts.[11] Following thermal oxidation, CuO doped porous ZnO nanobelts are successfully obtained, not Cu nanoparticle decorated porous ZnO nanobelts.

To obtain more detailed information about the microstructure of the as-prepared porous nanobelts, a high magnification TEM image of an individual porous CuO-doped ZnO nanobelt was obtained and is shown in Fig. 2a. It can be observed clearly that the synthesized porous nanobelts consist of numerous interconnected nanocrystals and nanopores. In the HRTEM image in Fig. 2b, two different lattice arrangements are displayed. One is the (002) lattice of ZnO with a plane distance of 0.26 nm, and the other corresponds to the (−111) lattice of CuO with a plane distance of 0.25 nm. Different from the previously reported pristine single-crystal porous ZnO nanobelts, the as-prepared porous CuO-doped ZnO nanobelts are polycrystalline, which can be inferred from their SAED pattern in the inset of Fig. 2b.[3d] This result may be attributed to the formation of CuO nanocrystals, which inhibits the formation of the regular single-crystal ZnO. Furthermore, these CuO nanocrystals are closely connected with ZnO nanocrystals and exist as a part of the nanobelts, and are not decorated on the surface of nanobelts. This leads to the formation of numerous heterojunctions among the as-prepared porous nanobelts. The elemental mapping patterns in Fig. 2c–e show that Zn, O and Cu elements are all uniformly distributed in the single porous nanobelt. This result strongly supports our initial idea that the partial cation-exchange strategy can be effectively applied to prepare uniform metal oxide-doped porous ZnO nanobelts.

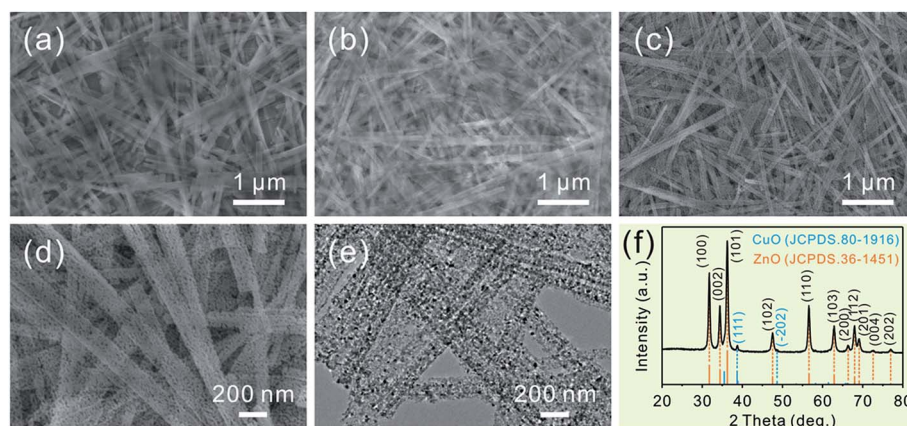To further confirm the composition evolution of precursor nanobelts during the above cation-exchange process and

Fig. 1 (a and b) SEM images of $ZnSe \cdot 0.5N_2H_4$ precursor nanobelts before and after partial exchange with Cu^{2+} cations, respectively; (c and d) low- and high-magnification SEM images of the as-prepared porous CuO-doped ZnO nanobelts, respectively; (e) their TEM image and (f) their XRD patterns.
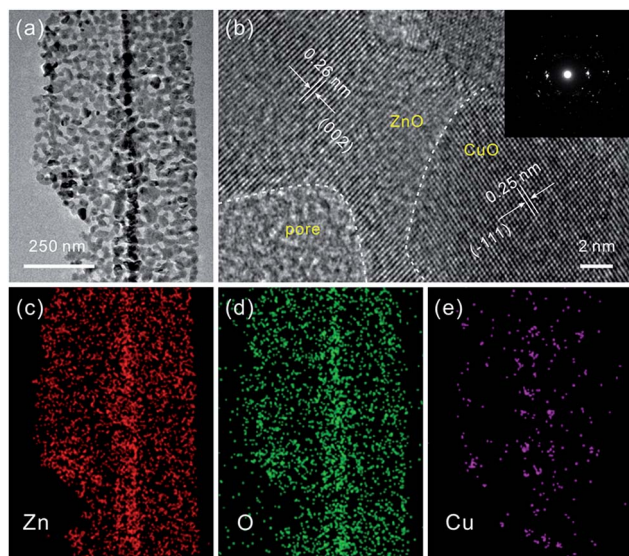
Fig. 2 (a) High-magnification TEM image of a single porous CuO-doped ZnO nanobelt, (b) its HRTEM image, wherein the inset corresponds to its SAED pattern, and (c)–(e) elemental mapping patterns of Zn, O and Cu elements of the single porous nanobelt, respectively.

thermal conversion, XPS characterization was performed. The complete XPS spectra are shown in Fig. 3a. After partial exchange with Cu^{2+} cations, peaks attributed to the Cu element emerged which were not observed in the spectrum of precursor nanobelts. In the high resolution XPS spectrum shown in Fig. 3b, two symmetric and narrow peaks centered at 932.3 eV and 952.2 eV are assigned to Cu $2p_{3/2}$ and Cu $2p_{1/2}$, respectively. This result is consistent with that of previously reported Cu_2Se

Fig. 3 (a) XPS spectra of $ZnSe \cdot 0.5N_2H_4$ precursor nanobelts before (I) and after (II) partial exchange with Cu^{2+} cations and the as-prepared porous CuO-doped ZnO nanobelts (III) after thermal oxidation, (b) XPS spectrum of Cu 2p of precursor nanobelts partially exchanged with Cu^{2+} cations, and (c) XPS spectrum of Cu 2p of porous CuO-doped ZnO nanobelts.

nanobelts, suggesting that Cu_2Se is formed and doped into precursor nanobelts.[9] After continuous calcination in air, the N peak completely disappeared, which is attributed to the thermal decomposition of N_2H_4 ligands. Additionally, the Se element is easily oxidized into SeO_2. Due to the fact that its sublimation temperature of about 315 °C is much lower than the 500 °C annealing temperature, the formed SeO_2 is rapidly and completely evaporated, leading to the disappearance of Se peaks. Notably, the high resolution XPS spectrum of Cu displayed in Fig. 3c shows that the Cu $2p_{3/2}$ and Cu $2p_{1/2}$ peaks are centered at 933.7 and 953.6 eV with a splitting of 19.9 eV, respectively. Clearly this is attributed to the presence of the Cu^{2+} chemical state.[12] Furthermore, the characteristic satellite peaks of Cu $2p_{3/2}$ and Cu $2p_{1/2}$ further confirm this result, and they are centered at 943.3 and 962.9 eV (∼9 eV greater than the corresponding major peaks), respectively.[13] Different from the high resolution XPS spectrum of Cu^+ shown in Fig. 3b, these results are greatly consistent with the widely reported XPS spectra of CuO.[14] The above analysis further confirms that Cu_2Se-doped precursor nanobelts were completely converted into CuO doped porous ZnO nanobelts after thermal oxidation.

Through manipulating the amount of exchanged Cu^{2+} cations, different concentrations of CuO-doping in ZnO porous nanobelts are obtained. In the following, a series of concentrations of Cu^{2+} cations were investigated such as 1, 2, 3, 4, and 5 at%. In SEM images shown in Fig. S1 (see the ESI†), it can be observed that the initial belt-like morphologies of the precursor are all preserved after exchange with different concentrations of Cu^{2+} cations. The color of the obtained sample gradually turns from milky white to brown, and it turns deeper and deeper with the increasing amount of exchanged Cu^{2+} cations. This phenomenon can be observed from optical images in the insets of Fig. S1 (see the ESI†). After annealing at 500 °C in air, all of them are further transformed into porous nanobelts, as shown in Fig. 4b–f. This result is well consistent with the pristine porous ZnO nanobelts shown in Fig. 4a. Based on the ICP measurements shown in Table S1 (see the ESI†), the final doping amounts of Cu are all fundamentally consistent with the theoretical values for the obtained porous nanobelts. This result confirms that the added Cu^{2+} cations were completely doped. XRD patterns in Fig. S2 (see the ESI†) correspond to the obtained porous ZnO nanobelts doped with different amounts of CuO. With the increase in the amount of the Cu element, diffraction peaks corresponding to CuO (JCPDS. 80-1916) clearly emerge and their intensity gradually increases. Moreover, no other peaks can be observed, indicating that there are no other impurities except CuO and ZnO.

Following the described experimental details, gas sensing devices based on porous nanobelts with different doping amounts of Cu have been successfully fabricated, as shown in Fig. S3a (see the ESI†). In the low- and high-magnification SEM images shown in Fig. S3b and c,† it can be seen that the obtained sensing film covering the ceramic substrate is porous and uniform. More importantly, the assembly approach along with *in situ* calcination preserves the belt-like morphology well and allows the porous nanobelts to sinter together. According to the cross sectional SEM image displayed in Fig. S3d,† the
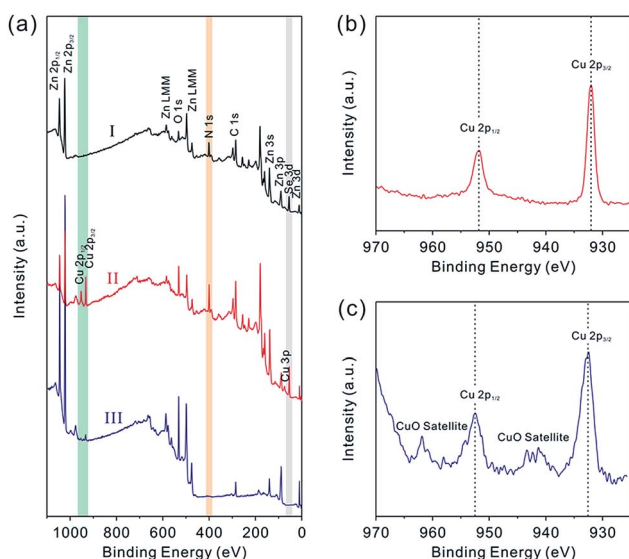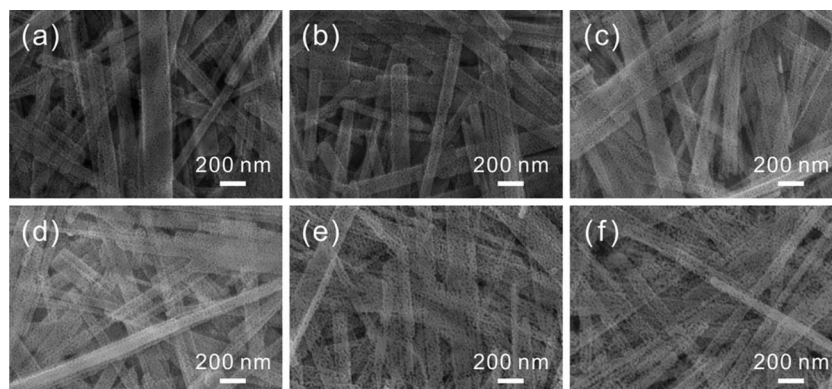
Fig. 4 SEM images of different amounts of porous CuO-doped ZnO nanobelts: (a) pristine porous ZnO nanobelts, (b) 1 at%, (c) 2 at%, (d) 3 at%, (e) 4 at%, and (f) 5 at%.

thickness of the fabricated sensing film is about 500 nm. In Fig. 5a, the relative responses are presented for different amounts of porous CuO-doped ZnO nanobelts toward 100 ppm of three typical VOCs such as propanol, acetone, and formaldehyde at a working temperature of 325 °C. Evidently, CZ-3 porous nanobelts (doped with 3 at% Cu) show a maximum relative response toward the VOCs. And maximum response values of 25, 50, and 22 are obtained towards propanol, acetone, and formaldehyde, respectively. The corresponding relative response curves toward propanol, acetone and formaldehyde are presented in Fig. S4a–c (see the ESI†), respectively. To optimize the working temperature, the sensing behaviors of CZ-

3 porous nanobelts (doped with 3 at% Cu) toward 100 ppm acetone were employed as an example and explored. For different operating temperatures, the corresponding relative response curves are displayed in Fig. S4d (see the ESI†). Based on the relationship curve shown in Fig. 5b, it can be observed that the relative response greatly increases with the working temperature from 225 to 325 °C. At 325 °C, the maximum relative response is obtained. Then it dramatically decreases from 325 to 375 °C. Evidently, this means that porous CuO-doped ZnO nanobelts exhibit the best sensing activity toward acetone at 325 °C. Therefore, their optimal working temperature is about 325 °C, which is selected to investigate the gas
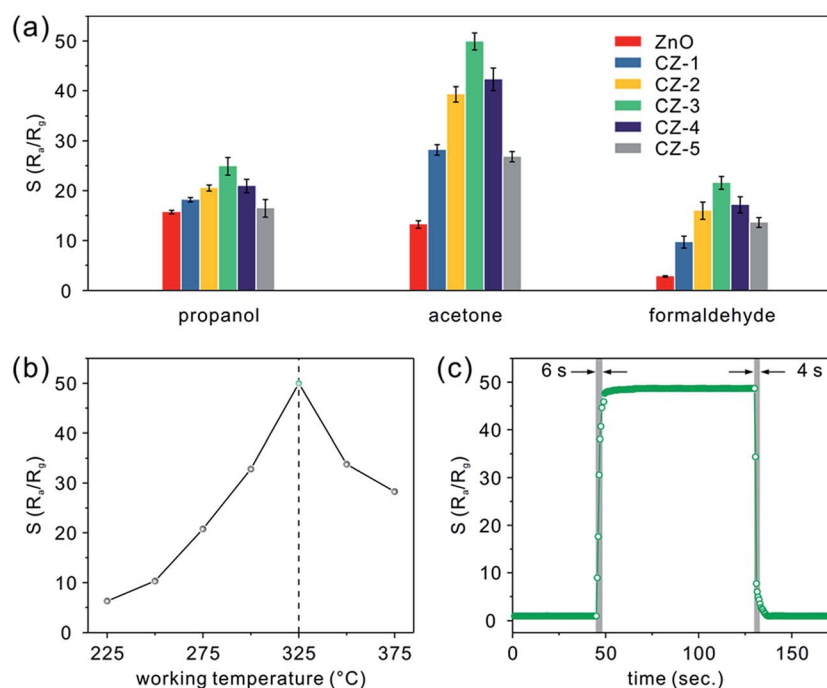

Fig. 5 (a) The relative responses of different amounts of porous CuO-doped ZnO nanobelts toward 100 ppm of three typical VOCs such as propanol, acetone, and formaldehyde at a working temperature of 325 °C, (b) the relationship between the relative response and working temperature of CZ-3 porous nanobelts toward 100 ppm of acetone, and (c) a typical real-time response curve of CZ-3 porous nanobelts toward 100 ppm of acetone at the optimal working temperature of 325 °C.

sensing performances. Fig. 5c shows a typical real-time response curve of CZ-3 porous nanobelts toward 100 ppm of acetone at the optimal working temperature of 325 °C. Clearly fast response and recovery times of about 6 and 4 s, respectively, were demonstrated. This result is mainly ascribed to the thin film consisting of porous nanobelts, which is favorable for the diffusion of acetone molecules.

As shown in Fig. 6a and b, the real-time response curves of CZ-3 porous nanobelts toward different concentrations of acetone have been investigated at the optimal working temperature of 325 °C. It can clearly be seen that all of them exhibit fast response and recovery. Fig. 6c and d show the corresponding relationship between the relative response and the concentration. Of particular importance, a good relative response was also shown to a low concentration of acetone in the range from 50 ppb to 2 ppm, as shown in Fig. 6b. These results can be ascribed to their special morphology, which is favorable for the diffusion of acetone molecules to effectively interact with all the nanostructures, leading to a greatly improved relative response. Notably, when the concentration of acetone is down to 50 ppb, they still show an obvious relative response.

Besides acetone, three other typical VOCs (ethanol, propanol and formaldehyde) were also measured. Fig. S5 (see the ESI†) shows the real-time relative response curves of CZ-3 porous nanobelts toward different concentrations of propanol, ethanol and formaldehyde at the optimal working temperature of 325 °C. Similarly, with an increase in their concentration, their relative responses also increase. From the corresponding relationship between the relative response and the concentration in

Fig. 7a, it can be observed that CZ-3 porous nanobelts exhibited the best relative response toward acetone. Compared with pristine porous ZnO nanobelts, CZ-3 porous nanobelts show better relative responses toward all investigated gases, as shown in Fig. 7b. Especially for ethanol, acetone and formaldehyde, the relative responses are more than two, four and ten times those of pristine porous ZnO nanobelts toward 100 ppm of each, respectively. These results suggest that the sensing activity of porous ZnO nanobelts is greatly enhanced after doping with CuO. Furthermore, the fabricated sensors based on CZ-3 porous nanobelts also show good reproducibility and stability. This result can be inferred from the almost identical relative responses toward 50 ppb of acetone obtained by repeating the test 20 times and the relative responses toward 100 ppm of acetone, ethanol, propanol and formaldehyde before and after 6 months, as shown in Fig. S6 (see the ESI†). The main reason lies in the fact that the sensing film constructed based on the assembly technique and in situ calcination approach is uniform and cannot be detached from the substrate. Additionally, the sensing film consisting of porous CuO-doped ZnO nanobelts is obtained at a calcination temperature of 500 °C, which is higher than the working temperature of 325 °C. Therefore, nanocrystals among porous CuO-doped ZnO nanobelts can be stable at the working temperature, ensuring that the morphology of porous nanobelts is fundamentally preserved. This means that the fabricated sensing film also has a stable sensitivity. As listed in Table S2 (ESI†), the as-prepared porous CuO-doped ZnO nanobelts presented a better sensing performance toward acetone in contrast to previous reports.
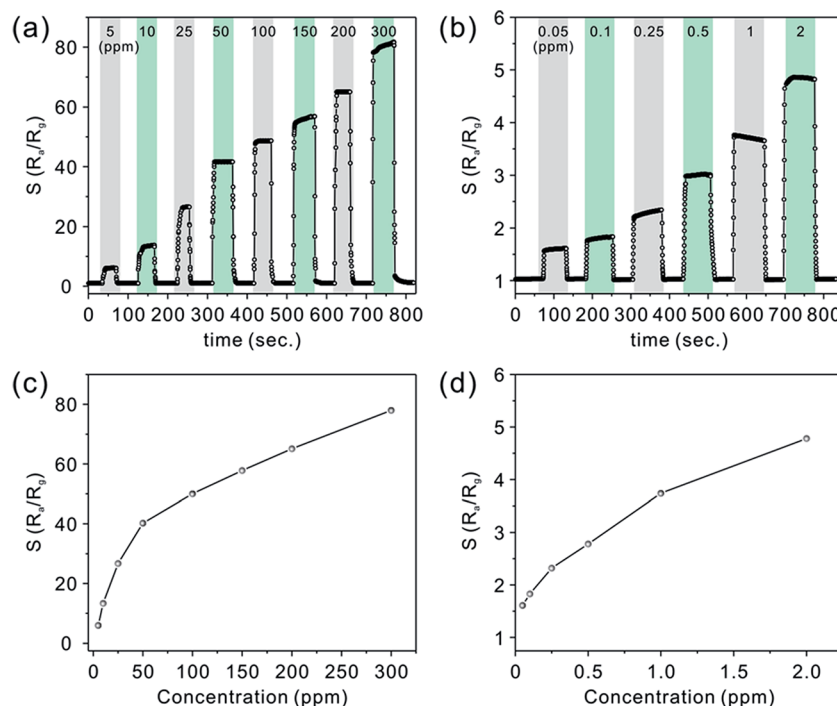

Fig. 6 (a and b) The real-time response curves of CZ-3 porous nanobelts toward different concentrations of acetone at the optimal working temperature of 325 °C, and (c and d) the relationship between the relative response and the concentration of acetone for CZ-3 porous nanobelts at the optimal working temperature of 325 °C.
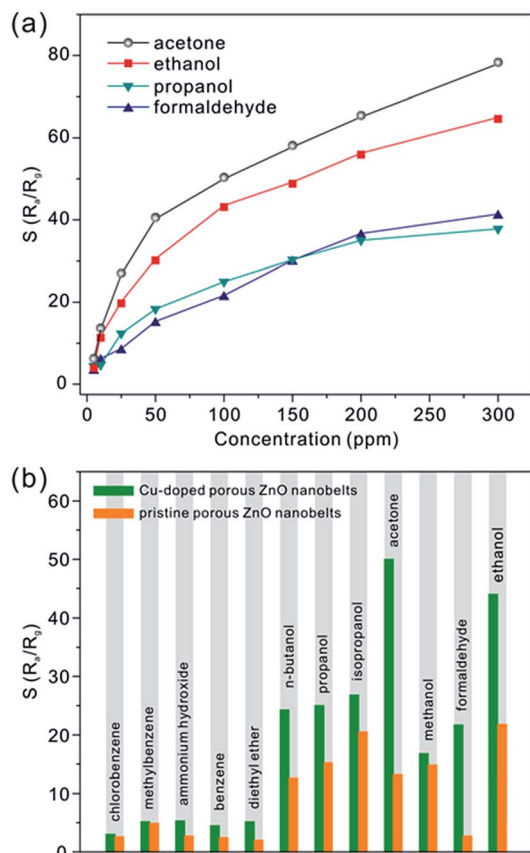
Fig. 7 (a) The relationship between the relative response and the concentration of some typical VOCs (acetone, ethanol, propanol, and formaldehyde), and (b) the relative responses of CZ-3 porous nanobelts toward all investigated VOCs (100 ppm) in contrast to those of pristine porous ZnO nanobelts at the optimal working temperature of 325 °C.

To shed light on the excellent gas-sensing performance described above, a possible sensing mechanism of porous CuO-doped ZnO nanobelts is offered, as shown in Fig. 8. As is well-known, the gas sensing performance of a semiconductor metal oxide mainly depends on the redox reaction between the target gas molecules and chemisorbed oxygen species (O^{2-}, O^- and O_2^-) on its surface.[15] Actually, it is attributed to the synergistic effect between the surface structure and electrical characteristics of the sensing materials. The sensing behaviors of porous CuO-doped ZnO nanobelts also abide by this principle.
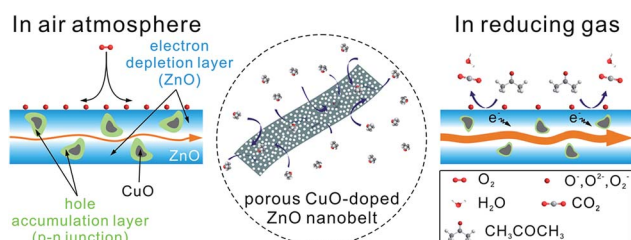

Fig. 8 Possible enhanced sensing mechanism for porous CuO-doped ZnO nanobelts.

Firstly their porous and belt-like structures provide more channels for the diffusion of gases and more active sites for the adsorption of gases and the reaction between the adsorbed oxygen ions and the detected gases. It will be beneficial to improve the sensitivity and shorten the response and recovery time. Secondly, among the self-assembly technique and *in situ* calcination, the assembly technique can afford a uniform and thin sensing film, effectively ensuring the fabrication repeatability of the sensing device, while the *in situ* calcination method can enable the nanobelts in contact to sinter together, greatly enhancing the stability of the fabricated sensing film.

Similar to that of pristine porous ZnO nanobelts, the resistivity of porous CuO-doped ZnO nanobelts still depends on the concentration of electrons as the major carrier. Differently, the as-prepared porous CuO-doped ZnO nanobelts contain numerous p–n heterojunctions at the interface between n-type ZnO and p-type CuO nanocrystals. When exposed to air, an electron depletion layer is formed due to the adsorption of oxygen species on the surface of porous ZnO nanobelts. Simultaneously, numerous local hole accumulation layers are formed around CuO nanocrystals, which is disadvantageous to electron transport.[16] This leads to the formation of a high barrier of p–n heterojunctions of CuO|ZnO. Undoubtedly, all this will contribute to the resistivity of porous CuO-doped ZnO nanobelts. After encountering acetone molecules as a representative reducing gas, the oxygen species adsorbed on the surface of porous nanobelts will react with them. The electrons captured by these oxygen species will be released back to the porous nanobelts, weakening the formed electron depletion layer. At the same time, the local hole accumulation layers will be thinned, weakening the barrier of p–n heterojunctions of CuO|ZnO. However, for pristine porous ZnO nanobelts, only the electron depletion layer is formed owing to the adsorption of oxygen species on their surface without forming local hole accumulation layers and p–n heterojunctions. The change of their resistivity varies only with the electron depletion layer. Therefore, compared with pristine porous ZnO nanobelts, the as-prepared porous CuO-doped ZnO nanobelts exhibit greater chemoresistive variation. Accordingly, the synergic effect between the formed electron depletion layer and the local hole accumulation layer greatly enhances the sensing response toward VOCs. Notably, the distributed density and size of CuO crystals greatly depend on their doping amount among the porous nanobelts. A higher number of CuO nanocrystals (corresponding to p–n heterojunctions) with smaller sizes is more favorable for improving sensing performances. Based on the results obtained above, we think that the number of CuO nanocrystals will increase with an increase in their doping amount when it is less than 3 at%. Above 3 at%, the distance among CuO nanocrystals will be smaller. During the annealing process the adjacent CuO nanocrystals will be easily sintered together, increasing their size and simultaneously decreasing the number of p–n heterojunctions. This will weaken its sensing activity. Based on the analysis above, the number of p–n heterojunctions and the size of CuO nanocrystals for 3 at% CuO dopant should be optimal to obtain the best relative response.

The selective enhancement toward ethanol, acetone and formaldehyde may be ascribed to the catalytic activity of CuO.[17]

Conclusions

In summary, well-defined porous CuO-doped ZnO nanobelts have been successfully prepared through a partial cation-exchange strategy in combination with thermal oxidation. The CuO-doping amount can be precisely tuned through manipulating the amount of exchanged Cu^{2+} cations. Additionally, the Cu element is uniformly distributed along the porous ZnO nanobelts. With the assembly technique and *in situ* calcination, a uniform and stable sensing film consisting of porous CuO-doped ZnO nanobelts has been achieved and shown to have an excellent sensing repeatability. Most importantly, porous CuO-doped ZnO nanobelts exhibit a better relative response toward VOCs in contrast to pristine porous ZnO nanobelts, especially toward ethanol, acetone and formaldehyde. The reason is mainly ascribed to the synergic effect between the formed electron depletion layer and the local hole accumulation layer at the p–n junctions of CuO|ZnO heterointerfaces. Among the investigated VOCs, the best relative response was achieved toward acetone with a low detection limit down to the ppb level. Owing to the thin sensing film with a porous structure, a fast response and recovery time of about 6 and 4 s was obtained toward 100 ppm of acetone, respectively. This work provides an effective strategy to prepare other uniform metal-doped ZnO nanobelts, even extending it to the construction of other uniformly doped porous metal oxide nanostructures with high sensing performance and catalytic activity.

Conflicts of interest

There are no conflicts to declare.

Acknowledgements

References

1 (a) V. Valtchev and L. Tosheva, *Chem. Rev.*, 2013, **113**, 6734; (b) Z. Guo, M. Q. Li and J. H. Liu, *Nanotechnology*, 2008, **19**, 245611; (c) Z. Guo, J. Y. Liu, Y. Jia, X. Chen, F. L. Meng, M. Q. Li and J. H. Liu, *Nanotechnology*, 2008, **19**, 345704; (d) S. Mariani, L. Pino, L. M. Strambini, L. Tedeschi and G. Barillaro, *ACS Sens.*, 2016, **1**, 1471; (e) H. Long, A. Harley-Trochimczyk, T. Y. He, T. Pham, Z. R. Tang, T. L. Sho, A. Zettl, W. Mickelson, C. Carraro and R. Maboudian, *ACS Sens.*, 2016, **1**, 339; (f) Z. Guo, M. L. Seol, M. S. Kim, J. H. Ahn, Y. K. Choi, J. H. Liu and X. J. Huang, *Nanoscale*, 2012, **4**, 7525.

2 Z. H. Jing and J. H. Zhan, *Adv. Mater.*, 2008, **20**, 4547.

3 (a) J. R. Huang, H. B. Ren, P. P. Sun, C. P. Gu, Y. F. Sun and J. H. Liu, *Sens. Actuators, B*, 2013, **188**, 249; (b) J. Y. Liu,
Z. Guo, F. L. Meng, T. Luo, M. Q. Li and J. H. Liu, *Nanotechnology*, 2009, **20**, 125501; (c) F. Meng, J. Yin, Y. Q. Duan, Z. H. Yuan and L. J. Bie, *Sens. Actuators, B*, 2011, **156**, 703; (d) X. B. Jin, Y. X. Li, Y. Su, Z. Guo, C. P. Gu, J. R. Huang, F. L. Meng, X. J. Huang, M. Q. Li and J. H. Liu, *Nanotechnology*, 2016, **27**, 355702; (e) P. P. Wang, Q. Qi, X. X. Zou, J. Zhao, R. F. Xuan and G. D. Li, *RSC Adv.*, 2013, **3**, 23980; (f) M. Chen, Z. H. Wang, D. M. Han, F. B. Gu and G. S. Guo, *J. Phys. Chem. C*, 2011, **115**, 12763; (g) C. P. Gu, J. R. Huang, Y. J. Wu, M. H. Zhai, Y. F. Sun and J. H. Liu, *J. Alloys Compd.*, 2011, **509**, 4499; (h) Z. T. Liu, T. X. Fan, D. Zhang, X. L. Gong and J. Q. Xu, *Sens. Actuators, B*, 2009, **136**, 499; (i) J. Zhao, X. X. Zou, L. J. Zhou, L. L. Feng, P. P. Jin, P. Liu and G. D. Li, *Dalton Trans.*, 2013, **42**, 14357; (j) Z. Wen, L. P. Zhu, L. Li, L. W. Sun, H. Cai and Z. Z. Ye, *Dalton Trans.*, 2013, **42**, 15551.

4 (a) C. P. Gu, H. H. Huang, J. R. Huang, Z. Jin, H. X. Zheng, N. Liu, M. Q. Li, J. H. Liu and F. L. Meng, *Sens. Actuators, A*, 2016, **252**, 96; (b) F. L. Meng, N. N. Hou, Z. Jin, B. Sun, Z. Guo, L. T. Kong, X. H. Xiao, H. Wu, M. Q. Li and J. H. Liu, *Sens. Actuators, B*, 2015, **209**, 975; (c) Y. H. Xiao, L. Z. Lu, A. Q. Zhang, Y. H. Zhang, L. Sun, L. Huo and F. Li, *ACS Appl. Mater. Interfaces*, 2012, **4**, 3797; (d) X. H. Liu, J. Zhang, L. W. Wang, T. L. Yang, X. Z. Guo, S. H. Wu and S. R. Wang, *J. Mater. Chem.*, 2011, **21**, 349; (e) H. F. Fu, X. Wang, P. Wang, Z. H. Wang, H. Ren and C. C. Wang, *Dalton Trans.*, 2018, **47**, 9014.

5 (a) A. Yu, J. S. Qian, H. Pan, Y. M. Cui, M. G. Xu, L. Tu, Q. L. Chai and X. F. Zhou, *Sens. Actuators, B*, 2011, **158**, 9; (b) J. R. Huang, Y. J. Dai, C. P. Gu, Y. F. Sun and J. H. Liu, *J. Alloys Compd.*, 2013, **575**, 115; (c) Q. Xiao and T. Wang, *Mater. Res. Bull.*, 2013, **48**, 2786; (d) G. X. Wan, S. Y. Ma, X. W. Sun, A. M. Sun, X. B. Li, J. Luo, W. Q. Li and C. Y. Wang, *Mater. Lett.*, 2015, **145**, 48.

6 (a) Z. W. Pan, Z. R. Dai and Z. L. Wang, *Science*, 2001, **291**, 1947; (b) Z. Guo, X. Chen, J. H. Liu and X. J. Huang, *Small*, 2013, **9**, 2678; (c) Y. S. Li, J. Xu, J. F. Chao, D. Chen, S. X. Ouyang, J. H. Ye and G. Z. Shen, *J. Mater. Chem.*, 2011, **21**, 12852; (d) Y. Cheng, P. Xiong, C. S. Yun, G. F. Strouse, J. P. Zheng, R. S. Yang and Z. L. Wang, *Nano Lett.*, 2008, **8**, 4179.

7 (a) R. Q. Song, A. W. Xu, B. Deng, Q. Li and G. Y. Chen, *Adv. Funct. Mater.*, 2007, **17**, 296; (b) J. B. Shen, H. Z. Zhuang, D. X. Wang, C. S. Xue and H. Liu, *Cryst. Growth Des.*, 2009, **9**, 2187.

8 (a) Z. Guo, M. Q. Li, J. H. Liu and X. J. Huang, *Small*, 2015, **11**, 6285; (b) Z. Guo, Y. Su, Y. X. Li, G. Li and X. J. Huang, *Chem.– Eur. J.*, 2018, **24**, 9877.

9 Y. Su, G. Li, Z. Guo, Y. Y. Li, Y. X. Li, X. J. Huang and J. H. Liu, *ACS Appl. Nano Mater.*, 2018, **1**, 245.

10 (a) L. De Trizio and L. Manna, *Chem. Rev.*, 2016, **116**, 10852; (b) X. H. Zhong, Y. Y. Feng, Y. L. Zhang, Z. Y. Gu and L. Zou, *Nanotechnology*, 2007, **18**, 385606; (c) Y. F. Yu, J. Zhang, X. Wu, W. W. Zhao and B. Zhang, *Angew. Chem., Int. Ed.*, 2012, **51**, 897.

11 G. Li, Y. Su, Y. Y. Li, Y. X. Li, Z. Guo, X. J. Huang and J. H. Liu, *Nanotechnology*, 2018, **29**, 445501.

12 K. Y. Lee, H. Hwang, D. Shin and W. Choi, *J. Mater. Chem. A*, 2015, **3**, 5457.

13 S. C. Hsieh, P. Y. Lin and L. Y. Chu, *J. Phys. Chem. C*, 2014, **118**, 12500.

14 (*a*) Y. Sakai, S. Ninomiya and K. Hiraoka, *Surf. Interface Anal.*, 2012, **44**, 938; (*b*) X. Liu, Y. Sun, M. Yu, Y. Yin, B. S. Du, W. Tang, T. T. Jiang, B. Yang, W. W. Cao and M. N. R. Ashfold, *Sens. Actuators, B*, 2018, **255**, 3384.

15 W. X. Jin, S. Y. Ma, Z. Z. Tie, J. J. Wei, J. Luo, X. H. Jiang, T. T. Wang, W. Q. Li, L. Cheng and Y. Z. Mao, *Sens. Actuators, B*, 2015, **213**, 171.

16 B. W. Zhang, W. Y. Fu, H. Y. Li, X. L. Fu, Y. Wang, H. Bala, X. D. Wang, G. Sun, J. L. Cao and Z. Y. Zhang, *Mater. Lett.*, 2016, **176**, 13.

17 P. Rai, S. H. Jeon, C. H. Lee, J. H. Lee and Y. T. Yu, *RSC Adv.*, 2014, **4**, 23604.